Journal of Power Sources 207 (2012) 150–159

Contents lists available at SciVerse ScienceDirect

Journal of Power Sources

journal homepage: www.elsevier.com/locate/jpowsour

A second nearest-neighbor embedded atom method interatomic potential for Li–Si alloys

Zhiwei Cui[a], Feng Gao[a], Zhihua Cui[b], Jianmin Qu[a,*]

[a] Department of Civil and Environmental Engineering, Northwestern University, Evanston, IL 60208, USA
[b] Complex System and Computational Intelligence Laboratory, Taiyuan University of Science and Technology, Taiyuan, Shanxi Province 030024, PR China

ARTICLE INFO

Article history:
Received 21 October 2011
Received in revised form 28 January 2012
Accepted 29 January 2012
Available online 6 February 2012

Keywords:
Li-ion battery
Li–Si alloy
Modified embedded atom method
Particle swarm optimization
Disordered–ordered transition

ABSTRACT

A second nearest-neighbor modified embedded atom method (2NN MEAM) interatomic potential for lithium–silicon (Li–Si) alloys is developed by using the particle swarm optimization (PSO) method in conjunction with *ab initio* calculations. It is shown that the new interatomic potential is capable of simulating the transition from disordered to ordered states of Li–Si crystalline structures, an indication of the stability and robustness of the interatomic potential at finite temperature. Examples are given to demonstrate that the new interatomic potential is also capable of predicting the material properties of both crystalline and amorphous Li–Si alloys, including the elastic modulus, compositional expansion, diffusivity of Li in Li–Si alloys, plastic yield strength, *etc.*

1. Introduction

Lithium (Li) ion batteries have gained tremendous attentions recently in high energy capacity, high operating voltage and low self-discharge energy storage devices [1]. For higher capacity Li-ion batteries, silicon (Si) is being considered as a promising anode material owing to its highest known theoretical charge capacity ($4200\,mAh\,g^{-1}$) [2,3]. However, the volume expansion of the Si anode can be as much as 400% after fully charged, which often leads fracture failure resulting in reduced battery life [4–6]. Such mechanical failure has been one of the major roadblocks that prevent the technology breakthroughs for large scale commercialization of Si-based anode Li-ion batteries.

Extensive numerical simulations [7–9] and microscopic analyzes [4,6,10–19] have confirmed that the insertion of Li ions into Si forms Li–Si alloys. Depending on the amount of Li, Li_xSi alloys of various compositions might be formed [10,11]. Volumetric expansion due to Li insertion has also been studied extensively both numerically [7,20] and experimentally [8,21–23]. Based on known compositions and their volume change with respect to Si lattice, many researchers [24–32] have computed the stresses generated during Li insertion.

Although many attempts have been made and several models have been developed for understanding the precise mechanisms of Li insertion/extraction, these models are still far from being quantitative and are not ready for design applications. For instance, some existing models predict the stress generated by Li insertion, but do not account for the effect of stress on the diffusion of Li. Without such two-way coupling, these exiting models are unable to simulate correctly the insertion of Li in the Si, thus cannot calculate the Li concentration accurately. Without such information, one cannot calculate the stresses correctly, nor can one predict the fracture of the Si anode. This is because Li concentration is non-uniform, and highly dependent on the diffusion of Li within the Si anode, which is strongly influenced by stress distribution [21,33]. Although some recent studies have attempted to investigate the effect of stress on Li diffusion [32–36], models used in these studies either did not account for the electrochemical driving forces for Li transport [37,38], or ignored the effect of shear stresses, or was based on small strain deformation.

More importantly, recent TEM *in situ* observations [39–41] show that during the first charge of a Si nanoparticle or nanowire, a sharp crystal/amorphous interface is formed that moves towards the center as the charge progresses. At some point, fracture occurs on the particle surface due to tensile hoop stress. However, none of the existing theories seems to be able to predict such failure process.

A key drawback of all the existing models is the lack of input from material composition and microstructure. In fact, all the available models are based on continuum mechanics. Yet, Li insertion is inherently atomistic, because the insertion of Li atoms into Si causes significant changes in the Si bond structure [42]. What this means is that care must be taken in developing continuum

* Corresponding author. Tel.: +1 847 467 4528.
E-mail address: j-qu@northwestern.edu (J. Qu).

0378-7753/$ – see front matter © 2012 Elsevier B.V. All rights reserved.
doi:10.1016/j.jpowsour.2012.01.145

models in order to account for such microstructural changes during insertion. Otherwise, continuum models would be unable to simulate certain physical phenomena such as phase transformation and fracture as observed in Li insertion.

Another major shortcoming of the existing continuum models is the lack of appropriate values for many of the physical properties in the model, such as the plastic yield strength of Li_xSi as a function of Li concentration, and the diffusivity of Li in Li_xSi and its dependence on the stress. In theory, these properties can be measured experimentally. In reality, such measurements are extremely cumbersome, and difficult to perform.

With recent advances in computational algorithms and computer hardware, atomistic level computations, such as molecular dynamic (MD) simulations have become an effective and efficient tool for simulating material behavior and for computing material properties. If done correctly, MD simulations can provide insightful information on the microstructural changes during deformation, and enhance our understanding of the failure mechanisms. We believe that many of the existing continuum models on Li insertion will benefit greatly from comparing with atomistic level simulations.

However, to conduct MD simulations, the first thing needed is a proper interatomic potential. At the present time, interatomic potentials for Li–Si alloys are not available. This is the major reason that no MD simulation results have been published in the open literature so far. In fact, Haftbaradaran et al. [34] had developed a continuum model for Li diffusion in Li_xSi alloys. To verify their continuum model, they have conducted MD simulations. However, because of the lack of interatomic potential for Li–Si alloys, their MD simulations were performed on the diffusion of hydrogen in single crystal fcc nickel.

Clearly, there is a critical need for developing an accurate and robust interatomic potential for conducting MD simulations of Li insertion into Si anode. The potential should be able to describe all the possible atomic interactions in all the possible crystal structures of Li_xSi, as well as the amorphous Li_xSi of any $0 < x < 4.4$. It should also provide stable solution at both room and elevated temperatures. Furthermore, the potential must be able to calculate accurately the basic properties of Li_xSi including the elastic constants, the lattice constants, the cohesive energies, *etc.*

Such an interatomic potential for Li_xSi will be a powerful tool. It enables us to validate the various continuum models on Li insertion. It can be used to estimate some of the material properties that are difficult to obtain experimentally. It gives us a mean to study the microstructural mechanisms of fracture and failure.

One of the most widely used interatomic potentials for metals is the modified embedded atom method (MEAM) potential first proposed by Baskes [43]. It has been used for a variety of fcc metals with great success. However, as pointed out recently by Lee et al. [44], the MEAM potential has some drawbacks when used for bcc crystal structures. For instance, the (1 1 1) surface energy was found to be smaller than that of (1 0 0) surface by the MEAM potential, which is contrary to experimental results or *ab initio* calculations. Also, the MEAM potential predicts that the most stable structure for Li is not bcc, which is obviously incorrect.

To better describe the bcc structure, Lee et al. [44] proposed the second nearest neighbor (2NN) MEAM interatomic potential, and demonstrated that it is better suited for the bcc structure. Since then, 2NN MEAM potentials have been developed for several elements and their alloys including silicon [45] and magnesium [46].

This paper describes the development of a 2NN MEAM potential for the Li_xSi alloys. Our general approach is to use data from existing experimental measurements and *ab initio* computations. Based on these data, the parameters in the 2NN MEAM potential will be optimized by the particle swarm optimization (PSO) [47–49] technique.

Before proceeding, however, we note that Li_xSi alloys are somewhat different from typical metal alloys in that they exhibit some behavior of ionic solids. For example, a number of investigators [50,51] have used first principles calculations to study the charge transfer in Li_xSi crystal structures. Their results reveal that Li atoms donate a certain amount of electrons to the Si atoms in all crystalline Li–Si phases. However, the charge carried by the Si atoms seems to differ depending on the Li concentration, and the crystalline structure. Furthermore, in a given Li–Si crystalline structure, the charge distribution among Si atoms may not be the same. This poses a fundamental question as to whether an interatomic potential exists that is universal to all the different compositions and structures of Li_xSi. Although the answer to this question is not clear at this point, our preliminary MD results, as discussed in this paper, do show good agreement with the experimental data or with the *ab initio* computations, indicating that charge transfer effect in Li_xSi may be neglected, and an accurate and robust interatomic potential might exist that can accurately predict the behavior of Li_xSi alloys under a wide range of conditions.

2. Methodology

2.1. 2NN MEAM potential

In a 2NN MEAM formulation, the total energy of a system is written as [45,52]

$$E = \sum_i \left[F_i(\bar{\rho}_i) + \frac{1}{2} \sum_{j(\neq i)} \varphi_{ij}(R_{ij}) \right], \tag{1}$$

where $F_i(\bar{\rho}_i)$ is the embedding function, $\bar{\rho}_i$ is the background electron density at the site where atom i occupies, and $\varphi_{ij}(R_{ij})$ is the pair interaction between atoms i and j at a distance R_{ij}. The background electron density $\bar{\rho}$ is composed of several partial electron density terms. Each partial electron density is a function of atomic configuration and atomic electron density. The atomic electron density is given by

$$\rho_j^{a(h)}(R_{ij}) = \rho_0 \exp\left[-\beta^{(h)} \left(\frac{R_{ij}}{r_e} - 1 \right) \right], \tag{2}$$

where ρ_0 is a scaling factor, $\beta^{(h)}$ are adjustable parameters and r_e is the nearest neighbor distance in the reference structure after equilibrium. In the 2NN MEAM, the energy per atom in the reference structure is estimated from a universal equation of state [53]. Once $F_i(\bar{\rho}_i)$ is known, the pair potential $\varphi_{ij}(R_{ij})$ can be evaluated. More details of the MEAM formulation can be found in [45,52].

For a binary intermetallic compound, the only unknown function in the potential is the pair potential function between the different types of atoms. To obtain the pair potential function, the atoms that have the same type of atoms as second nearest-neighbors are considered as a reference structure. For the Li_xSi alloy considered here, we used a Li_3Si-type $L1_2$ ordered structure as the reference structure. Thus, the total energy per atom (for 3/4 Li atom + 1/4 Si atom) is given by,

$$E^u_{Li_3Si}(R) = \frac{1}{4}F_{Si}(\bar{\rho}_{Si}) + \frac{3}{4}F_{Li}(\bar{\rho}_{Li}) + \frac{Z_1}{2}\left[\frac{1}{2}\varphi_{SiLi}(R) + \frac{1}{2}\varphi_{LiLi}(R)\right] + \frac{Z_2}{2}\left[\frac{1}{4}S_{Si}\varphi_{SiSi}(aR) + \frac{3}{4}S_{Li}\varphi_{LiLi}(aR)\right], \tag{3}$$

where Z_1 and Z_2 are the numbers of first and second NN, respectively, in the $L1_2$ Li_3Si structure, S_{Li} and S_{Si} are the screening function for the 2NN interactions between Li, and Si atoms, respectively, and a is the ratio between the second and first NN distances in the reference structure. The pair potential function between Li

and Si can then be evaluated by

$$\varphi_{\mathrm{LiSi}}(R) = \frac{1}{3}E^{u}_{\mathrm{Li_3Si}}(R) - \frac{1}{12}F_{\mathrm{Si}}(\bar{\rho}_{\mathrm{Si}}) - \frac{1}{4}F_{\mathrm{Li}}(\bar{\rho}_{\mathrm{Li}}) - \varphi_{\mathrm{LiLi}}(R) - \frac{1}{4}S_{\mathrm{Si}}\varphi_{\mathrm{SiSi}}(aR) - \frac{3}{4}S_{\mathrm{Li}}\varphi_{\mathrm{LiLi}}(aR). \quad (4)$$

The only unknown term on the right hand side of (4) is the total energy per atom, $E^{u}_{\mathrm{Li_3Si}}$. To obtain $E^{u}_{\mathrm{Li_3Si}}$, the universal equation of state can be used. For the $L1_2$ structure of Li_3Si,

$$E^{u}_{\mathrm{Li_3Si}}(R) = -E_c[1 + a^* + d(a^*)^3]e^{-a^*}, \quad (5)$$

where

$$a^* = \alpha\left(\frac{R_{ij}}{r_e} - 1\right), \quad \alpha = \sqrt{\frac{9B\Omega}{E_c}} \quad (6)$$

In the above, r_e is the equilibrium NN distance, d is an adjustable parameter, B is the bulk modulus, and Ω is the equilibrium atomic volume. Once these parameters are determined for the $L1_2$ structure, the corresponding pair potential function φ_{LiSi} can be evaluated from (4).

In addition to these 4 parameters in the universal equation of state, there are 9 other parameters in the potential that need to be determined. One is the atomic electron density scaling factor ρ_0. It has been found that ρ_0 has little impact on pure element, but plays a significant role in alloys [44,45]. Furthermore, C_{max} and C_{min} are also crucial in determining the interaction range of the alloys. For Li–Si binary alloy system, there are 4 combinations of both C_{max} and C_{min}, *i.e.* (Li–Si–Li, Li–Li–Si, Si–Si–Li, Si–Li–Si) for a total of 8 parameters. Altogether, there are 13 parameters that can be adjusted in order to fit the 2NN MEAM potential for a binary alloy. They are E_c, r_e, α, d, ρ_0, and 4 combinations of both C_{max} and C_{min}. For a given set of these 13 parameters, a number of physical properties of the five known crystalline structures of Li_xSi alloys (x = 1, 12/7, 13/4, 15/4, 22/5), such as the lattice constants, cohesive energies, elastic constants, *etc.*, can be predicted by MD simulations. By fitting these MD predictions to their corresponding values from either experimental measurements or *ab initio* simulations, the 13 adjustable parameters in the 2NN MEAM potential can be optimized to yield an accurate and hopefully robust interatomic potential for the Li–Si alloys. In the next section, we will describe how such optimization can be accomplished by the PSO method.

To obtain the complete 2NN MEAM potential for the Li_xSi alloys, the corresponding potentials for Li and Si are also needed. The 2NN MEAM potential for pure Si has been obtained by Lee [45]. We have modified Lee's potential slightly so it is better suited for developing the 2NN MEAM potential for the Li–Si system, see Appendix A. The 2NN MEAM potential for Li was also developed earlier by the present authors [52].

2.2. Optimization procedures

In this section, we describe how the particle swarm optimization (PSO) method [47–49] can be used to determine simultaneously the 13 adjustable parameters in the 2NN MEAM potential. The PSO method is a novel population-based optimization technique. It was developed initially to simulate animal social behaviors, *e.g.*, birds flocking, fish schooling and insects herding. Due to its simple algorithm and fast convergence, the PSO has been widely adopted in many areas such as power system [54], structural damage identification [55], nonlinear system identification [56], ice-storage air conditioning system [57], *etc.*

The PSO method starts with a group (called swarm) of candidate solutions (called particles). These particles move around within the search space to seek food (called optimum). Let $\Pi(j)$ be an objective function that transforms a particle to a unique real number. The goal is to find a particular particle j such that $\Pi(j) \le \Pi(k)$ for all particle k within the search space.

Let $\mathbf{x} = (x_1, x_1, \ldots, x_M)$ represent a set of candidate parameters in the 2NN MEAM for a specific material. Thus the objective function for the optimization can be defined as,

$$\Pi(\mathbf{x}) = \sum_{i=1}^{N}\sigma_i\left[\frac{f_i(\mathbf{x})}{y_i} - 1\right]^2, \quad (7)$$

where $f_i(\mathbf{x})$ is a physical property calculated by MD simulations using the 2NN MEAM potential with the parameter set $\mathbf{x}$. Such physical properties can be, for example, lattice constants or elastic constants. The y_i is the corresponding value of the same physical property from *ab initio* calculations, or experimental measurements. The weighting factor σ_i is a positive number selected based on the importance of this particular physical property. In this study, structural properties are considered much more important than auxiliary structures, so they are given much larger weights. The objective here is to find a particular $\mathbf{x}_0$ so that $\Pi(\mathbf{x}_0) \le \Pi(\mathbf{x})$ for all $\mathbf{x}$ in the search space.

To start the optimization, each parameter is assigned a random value as the initial input. Physical properties of the systems are then computed based on the 2NN MEAM potential with this initial set of parameters. This gives the first iteration of $f_i(\mathbf{x})$ in Eq. (7). The next set of candidate parameters is then selected using the PSO algorithm. A small enough "time step" is used in the PSO to ensure that each partial electron density term has the same order of magnitude. The above procedures are repeated until the objective function $\Pi(\mathbf{x})$ has been minimized to a satisfactory level. All the MD simulations in this study are conducted by using the LAMMPS software code [58,59].

As seen from Eq. (7), a database of physical properties y_i is needed in order to optimize the parameters in the 2NN MEAM potential. In this work, the physical properties used include the lattice constants, cohesive energies and elastic constants for 5 Li_xSi alloy structures (x = 1, 12/7, 13/4, 15/4, 22/5, corresponding to Li_1Si_1, $Li_{12}Si_7$, $Li_{13}Si_4$, $Li_{15}Si_4$, and $L_{22}Si_5$, respectively), as well as the binding energies of five auxiliary structures, namely, four crystals (B1, B2, B3, L12) and one molecular structures (LiSi). These properties are either calculated by *ab initio* simulations carried in this work or obtained from the open literature.

The *ab initio* calculations are performed using the CASTEP software [60]. The ultrasoft pseudopotentials are used in conjunction with the Perdew–Burke–Ernzerhof (PBE) generalized gradient approximations (GGA) exchange correlation function. The cutoff of plane-wave basis set is 500 eV atom^{-1}. The energy tolerance for the self-consistent field convergence is 5.0×10^{-7} eV atom^{-1} for all the calculations.

The optimized parameters obtained from the procedures described above are listed in Table 1. Making use of these

Table 1
Optimized parameters in the 2NN MEAM potential for Li–Si alloys.

Parameters	
E_c (eV atom^{-1})	2.45
r_e (Å)	2.75
α	4.10
d	0.10
ρ_0 ($\rho_0^{\mathrm{Si}}/\rho_0^{\mathrm{Li}}$)	3.0
C_{max} (Li–Li–Si)	2.81
C_{max} (Si–Si–Li)	2.20
C_{max} (Li–Si–Li)	2.40
C_{max} (Li–Si–Si)	2.40
C_{min} (Li–Li–Si)	0.55
C_{min} (Si–Si–Li)	0.35
C_{min} (Li–Si–Li)	0.45
C_{min} (Li–Si–Si)	0.45

Table 2
Physical properties of 5 Li_xSi crystal structures using the new 2NN MEAM potentials. The units of the cohesive energy (E_c), equilibrium lattice constants (A, B and C) and elastic constants (C_{11}–C_{66}) are in eV, Å and GPa, respectively. The first row of each alloy system is from our MD simulations, and the second row is from our *ab initio* calculations.

	E_c	A	B	C	C_{11}	C_{22}	C_{33}	C_{12}	C_{13}	C_{23}	C_{44}	C_{55}	C_{66}
Li_1Si_1	3.333	9.346	9.346	5.673	112	112	94	58	72	72	42	42	26
	3.301	9.356	9.356	5.742	101	101	77	19	37	37	45	45	37
$Li_{15}Si_4$	2.361	10.589	10.589	10.589	48	48	48	33	33	33	23	23	23
	2.466	10.616	10.616	10.616	47	47	47	21	21	21	28	28	28
$Li_{22}Si_5$	2.270	18.776	18.776	18.776	52	52	52	28	28	28	30	30	30
	2.353	18.680	18.680	18.680	46	46	46	23	23	23	35	35	35
$Li_{12}Si_7$	2.855	8.139	20.358	14.343	87	78	85	45	42	39	17	20	15
	2.950	8.553	19.647	14.317	92	97	90	5	11	8	28	26	24
$Li_{13}Si_4$	2.412	7.993	15.103	4.427	75	70	74	22	24	28	20	14	14
	2.556	7.932	15.105	4.437	74	61	77	17	11	10	23	24	28

parameters in Eq. (1), one obtains the 2NN MEAM interatomic potential for Li–Si alloys.

2.3. Validity and accuracy of the new 2NN MEAM potential for Li_xSi

To assess the accuracy of the new potential, we have calculated several physical properties of Li_xSi alloys. Shown in Table 2 are the properties of crystalline Li_xSi alloys calculated by *ab initio* simulations, as well as the MD results by using the 2NN MEAM potential for Li–Si. It is seen that, using the 2NN MEAM potential in conjunction with the parameters listed in Table 1, the MD simulations predict these physical properties very well.

Another comparison is shown in Fig. 1, where the MD results based on the new 2NN MEAM potential are shown together with the *ab initio* results for the binding energies of 5 auxiliary structures. Overall, the average difference is estimated to be less than 10%, expect for the "Dimer" structure which gives a relatively higher value, ~60%.

Another important validation of interatomic potentials for crystalline materials is their ability to simulate the transition from a disordered structure to an ordered structure[52]. To this end, MD simulations are conducted using the new 2NN MEAM potential to simulate the transition of several Li–Si alloys from disordered structures to crystalline structures. The disordered structures are obtained by creating an offset (*ca.* 0.75 Å) from the original sites of the atoms. Fig. 2a shows a typical disordered structure of $Li_{22}Si_5$. Next to it, the corresponding radial distribution function (RDF) is plotted, which clearly indicates a disordered structure. From this initially disordered structure, MD simulations are conducted to equilibrate the system. During the equilibration, the structure gradually becomes more and more ordered and eventually returns back to its original crystalline structure with cohesive energy and lattice constants identical to the original ordered structure. Fig. 2b–d shows several snapshots of the structure and the corresponding RDF during the equilibration. Such transition can be considered as a specific transition path from the molten state to a solid state, which in turn proves that the newly developed 2NN MEAM potential is robust.

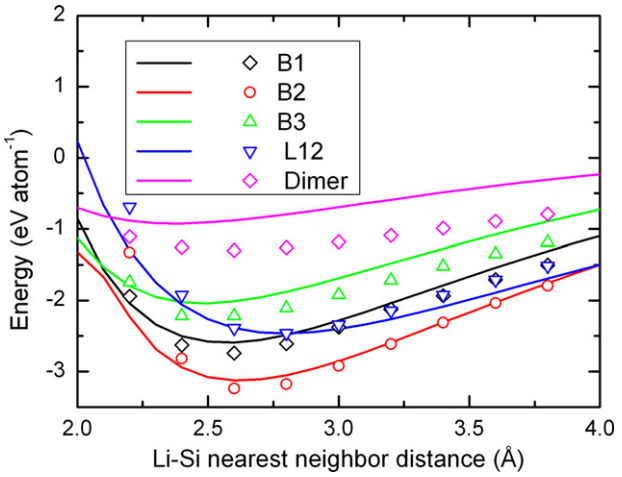

Fig. 1. Comparison between our MD simulations (data points) and *ab initio* calculations (solid curve). Energies of several crystals and molecular structures are plotted *versus* the Li–Si nearest-neighbor distance.

3. Properties of amorphous Li_xSi alloys

In this section, properties of Li_xSi alloys will be computed using MD simulations based on the 2NN MEAM interatomic potential developed in the previous section. The first step in MD simulation is to construct a simulation cell with atomistic structure identical to that of the material being simulated. This is usually easy for crystalline materials. However, it is not so trivial for amorphous materials. In this work, we create the amorphous structure *via* a rapid quench process – increasing the temperature of an initially crystalline structure of a given composition to 4000 K; then decreasing the temperature rapidly to room temperature. Such rapid quenching creates an amorphous structure with desired composition. The amorphous nature of the resulted simulation cells is demonstrated by the RDF shown in Fig. 3 for all Li_xSi alloys studied in this work. It is clearly seen that the simulations cells created by the rapid quenching are indeed amorphous. In all these alloys, the first neighbor distance varies from 2.75 to 2.90 Å for Li–Li with the increment of Li concentration, while it remains constant (*i.e.*, 2.67 Å) for Li–Si. One interesting observation is that the Si atoms seem to be much less disordered than the Li atoms, which indicates some Si atoms are still covalently bonded whereas with slightly larger bond distance varying from 2.35 to 2.54 Å after lithiation. Overall, our results are in good agreement with the recent *ab initio* studies [51,61].

Once the simulation cell is constructed, MD simulations can be performed. Unless stated otherwise, MD simulations in this paper are conducted on the NPT ensemble at finite temperature by using the Nose-Hoover thermostat and Parrinello-Rahman pressostat. The cutoff distance is set up as 4.8 Å. Time step is set as 1fs. Each simulation starts with 1000 ps equilibrium, followed by an additional 2000 ps for data collection.

3.1. Coefficient of compositional expansion (CCE) of amorphous Li_xSi alloys

The coefficient of compositional expansion (CCE) due to Li insertion can be calculated by the linear strain per lithium concentration [62,63],

$$\eta = \left.\frac{\partial \varepsilon_L}{\partial x}\right|_{x=x_0}, \tag{8}$$

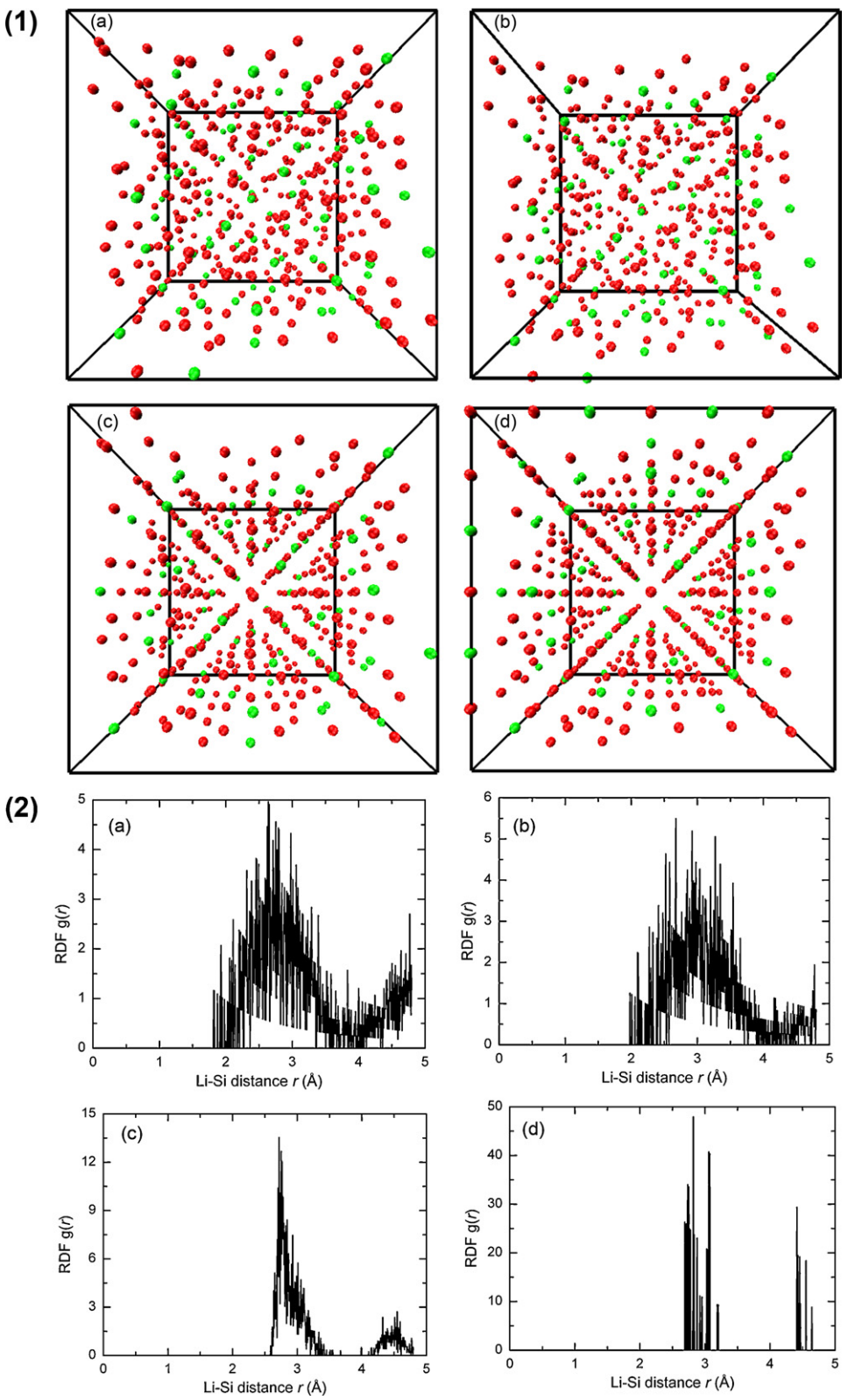

Fig. 2. Several typical snapshots of intermediate structures and corresponding RDFs during the transition from disordered (a) to ordered states (d).

where ε_L is the linear compositional expansion and x is the lithium concentration. The strain of an amorphous structure arising from the solute concentration change is purely volumetric and isotropic. Thus the linear strain of amorphous Li_xSi alloy can be written as

$$\varepsilon_L = \frac{V(x) - V(0)}{3V(0)}, \tag{9}$$

where V_0 is the volume of crystalline silicon. In this paper, the volume change $V(x)$ is computed by conducting MD simulations

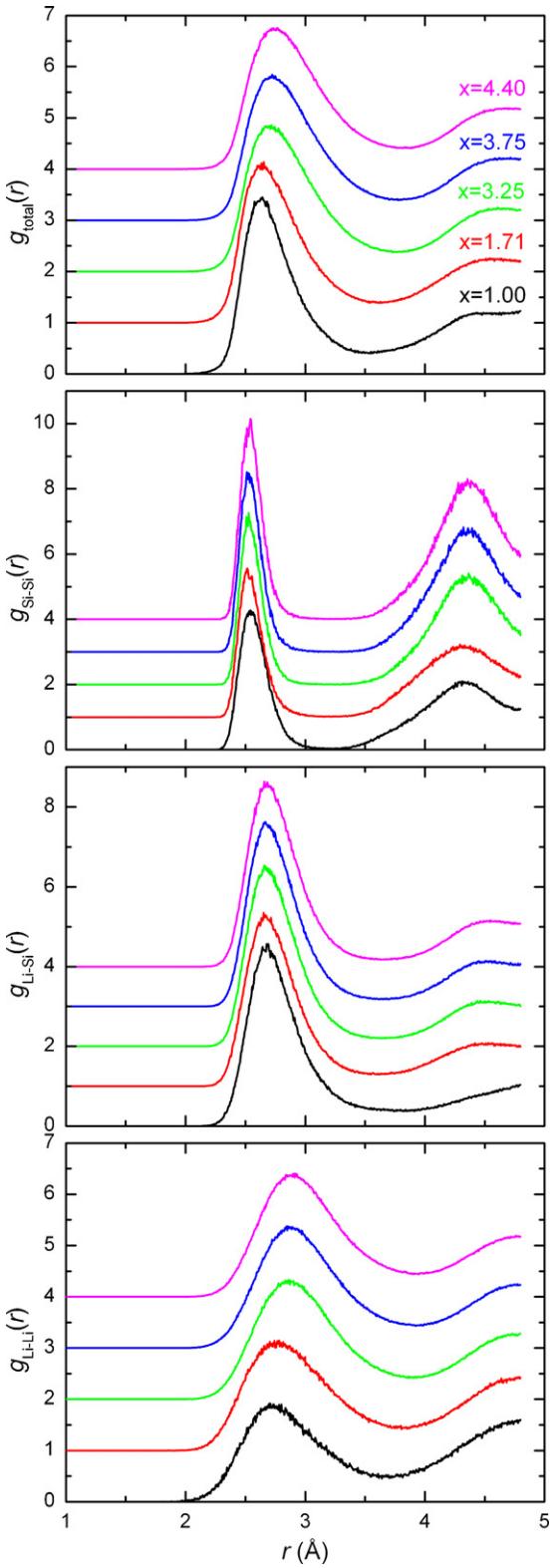

Fig. 3. Radial distribution functions of Li_xSi amorphous alloys created by quenching.

using the 2NN MEAM potential developed in the previous section. Shown in Fig. 4 is the computed volume expansion *versus* lithium concentration in Li_xSi. The results agree well with the *ab initio* calculations and experimental measurements. For example, for $x = 3.75$, our result is 3.9, while the *ab initio* value is 4.1 [42], and the experimental data ranges from 3.6 to 5.4 [41]. Making use of these results in Eq. (8) yields $\eta = 0.2555$.

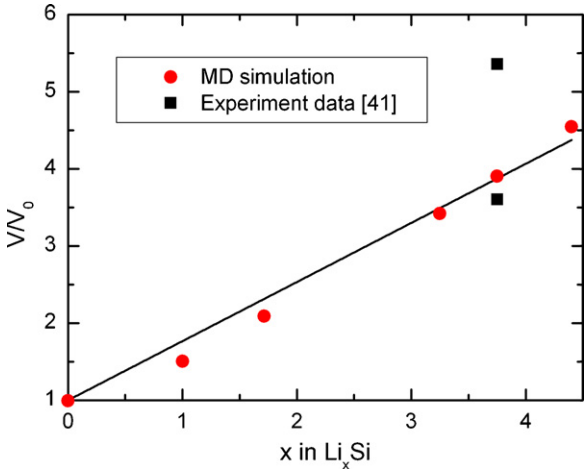

Fig. 4. Volume change *versus* lithium concentration. Experimental results are evaluated from [41].

3.2. Elastic modulus of amorphous Li_xSi alloys

Elastic constants of amorphous Li_xSi alloys are calculated from MD simulations by using the stress and strain fluctuation formula [64]. The results show that the calculated elastic stiffness tensor is isotropic, as expected from the amorphous structure. Four elastic constants (only two of them are independent) are shown in Fig. 5. For pure amorphous Si ($x = 0$) at room temperature, the elastic modulus of our MD result is 116 GPa, slightly larger than the experimental measurement (90–110 GPa) [65], while the shear modulus (46 GPa) is within the range of available experimental values (45–56 GPa) [65]. For the amorphous alloys, neither experimental nor simulated room temperature data are available in the literature. For comparison, we also calculate the modulus at 0K, which is plotted in Fig. 5 (solid black squares) against the corresponding *ab initio* results (open diamonds) from [20]. It seems that our MD simulations predict stiffer bulk and Young's moduli than the *ab initio* calculations from [20], especially for pure amorphous Si. We do note here, however, that our 0K modulus for pure amorphous Si agrees well with other *ab initio* studies, *e.g.* [66] and empirical calculations [67].

To use the concentration dependent modulus in a continuum thermodynamic model, the following expressions for the Young's modulus $E(x)$ and the Poisson's ratio $\nu(x)$ may be used,

$$E(x) = E(0)(1 + \eta_{E1}x + \eta_{E2}x^2), \quad \nu(0) = \nu(0)(1 + \eta_{\nu 1}x + \eta_{\nu 2}x^2), \tag{10}$$

where $E(0) = 102.6$ GPa is the Young's modulus of pure amorphous Si, $\eta_{E1} = -0.41$, $\eta_{E2} = 0.047$, $\nu(0) = 0.30$ is the Poisson's ratio of pure amorphous Si, $\eta_{\nu 1} = 0.16$, and $\eta_{\nu 2} = -0.018$. These values are obtained by fitting the quadratic equations to our MD data shown in Fig. 5.

3.3. Composition-dependent diffusivity of Li in Li_xSi alloys

The diffusivity of Li in the Li_xSi alloys depends on the composition of the alloys [68]. To investigate such dependence, MD simulations are conducted to calculate the mean square displacement (MSD). MSD has been extensively used to describe the movement of atoms in solids, liquids and gases. Obviously, the MSD also contains information on the diffusion of atoms. It has been shown that the MSD increases linearly with time when diffusion occurs [69], and the slop of the MSD *versus* time curve gives the

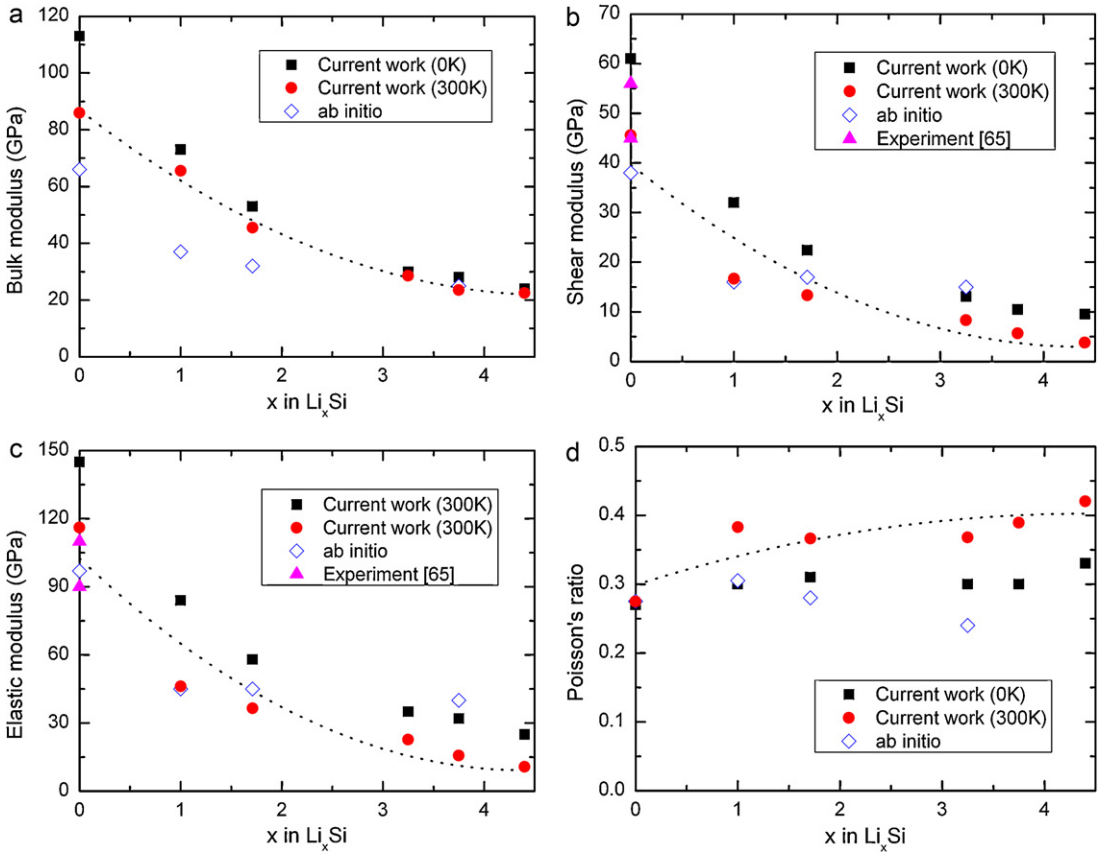

Fig. 5. Elastic constants of five Li_xSi amorphous structures obtained from the new 2NN MEAM potentials at 0 K and 300 K. Dotted lines are used for visual convenience. Experimental results are from [65].

diffusion constant D,

$$D = \frac{1}{6}\lim_{\Delta t\to\infty}\frac{\mathrm{MSD}(t+\Delta t)-\mathrm{MSD}(t)}{\Delta t} = \frac{1}{6}\lim_{t\to\infty}\frac{\left\langle\left|\mathbf{r}_i(t+\Delta t)-\mathbf{r}_i(t)\right|^2\right\rangle}{\Delta t}, \quad (11)$$

where $\mathbf{r}_i(t)$ is the position vector of the diffusing atom i at the time t, and the symbol $\langle\rangle$ denotes the average over all the diffusing atoms in the simulation cell. Theoretically, the MSD(t) is a linear function of t so that the D calculated from Eq. (11) is independent of t. In reality, there are always fluctuations in the MSD(t) when calculated by MD simulations. Thus, linear regression, instead of numerical derivative, is used to calculate the diffusivity D from the MSD(t) curve.

Another challenge is computing MSD at room temperature. Because the diffusion of Li at room temperature is rather slow, it is extremely time consuming to conduct MD in order to calculate MSD, particularly at lower Li concentrations. Therefore, we compute the MSD at elevated temperature in this work. An example is shown in Fig. 6 where the MSD of Li atoms in Li_1Si_1 is plotted as a function of t at several elevated temperatures. From these high temperature data, diffusivity at temperatures can be obtained from (11). Once the diffusivity is known at several higher temperatures, its room temperature value can be extrapolated through the following Arrhenius equation,

$$D(T) = D_0 \exp\left(\frac{-E_a}{RT}\right), \quad (12)$$

where T is the absolute temperature, R is the universal gas constant, and D_0 and E_a are constants independent of temperature. In fact, the high temperature data show a linear relationship between ln(D) and ($1/T$), as shown by the solid dots in Fig. 7.

Using the method described above, we have calculated the room temperature (300 K) diffusivity of Li and Si in both crystalline and amorphous Li_xSi for several values of x. The results are shown in Fig. 8a for Li and Fig. 8b for Si. Several observations can be made. First, the diffusion of Li in Li_xSi alloy is at least an order of magnitude faster than that of Si, indicating that Li is the dominant diffusing species. Second, the diffusivity of Li either or Si is orders of magnitude smaller in crystalline Li_xSi than that in the corresponding amorphous alloy, with the exception of Li in $Li12_2Si_7$, where the difference is much smaller. This is supports the hypothesis used

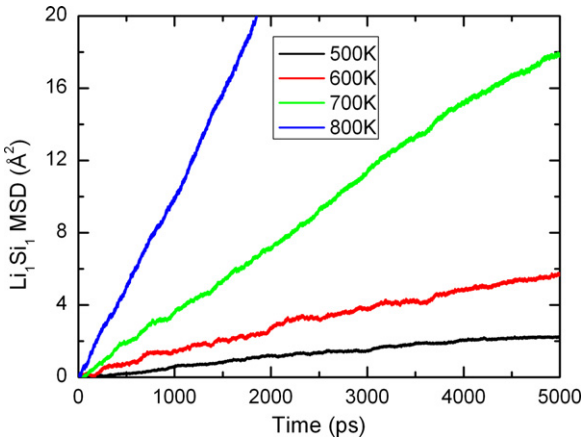

Fig. 6. MSD of Li atoms in a Li_1Si_1 simulation cell under different temperatures.

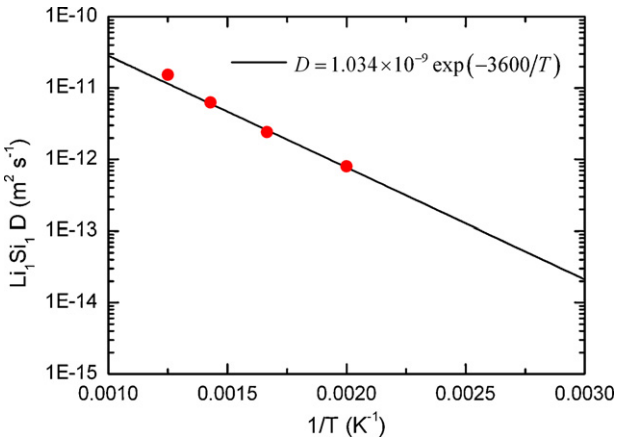

Fig. 7. Diffusivity is related to temperature through the Arrhenius equation. The solids dots are calculated directly from the high temperature MSD data.

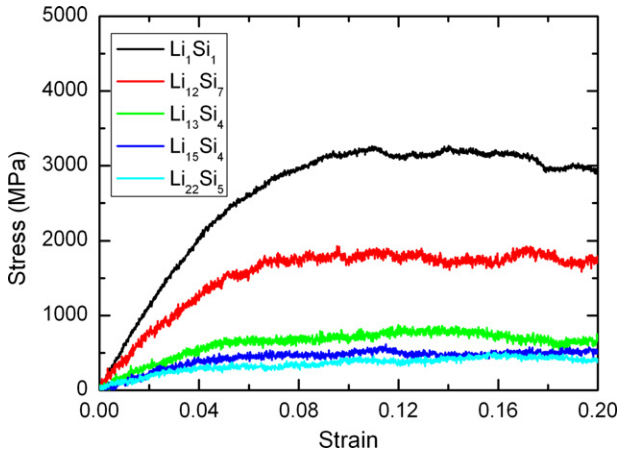

Fig. 9. Uniaxial stress–strain curves of amorphous Li_xSi alloys at 300 K under the strain rate of 10^8.

in Ref. [70] that the large difference in diffusivity between the amorphous and the crystalline structures is a major cause of the observed radial cracking of Si particles and wires [39]. Third, in the amorphous Li_xSi alloys, diffusivity of Li increases dramatically and monotonically as the Li concentration increases; in the crystalline Li_xSi alloys, however, the diffusivity of Li first increases with increasing Li concentration, then starts to decrease as Li concentration increases further. The highest diffusivity of Li seems to occur in $Li_{13}Si_4$. Finally, we note that similar trend can also be observed for the diffusivity of Si, although the highest diffusivity of Si occurs in $Li_{12}Si_7$.

It is noted that the Li diffusivity in amorphous Li_1Si_1 shown in Fig. 8 is smaller than the recent *ab initio* calculation [61] in which the mixing process is studied. In addition, our Li diffusivity is much higher than the experimental data [68], and shows a monotonic increase with increasing *x*, while the experimental data seem to exhibit a "W" shape with two minimum regions at $Li_{2.1\pm0.2}Si$ and $Li_{3.2\pm0.2}Si$. These differences might be attributed to the possible coexistence of amorphous and crystalline microstructures in the partially lithiated experimental samples. Further studies are being conducted to reconcile the differences.

3.4. Uniaxial stress–strain relationship at 300 K

To understand the mechanical behavior, MD simulations at 300 K are conducted to obtain the room temperature uniaxial stress–strain relationship for amorphous Li_xSi alloys. The simulations using the NPT ensemble are carried out on an amorphous Li_xSi supercell by applying a constant strain rate uniaxially. Periodic boundary conditions (PBC) are prescribed in all three directions of the simulation cell. Traction on the surfaces normal to the loading direction is set to zero to ensure that the deformation is uniaxial. To explore the strain rate effect, three rates, 10^7, 10^8, and 10^9, are used.

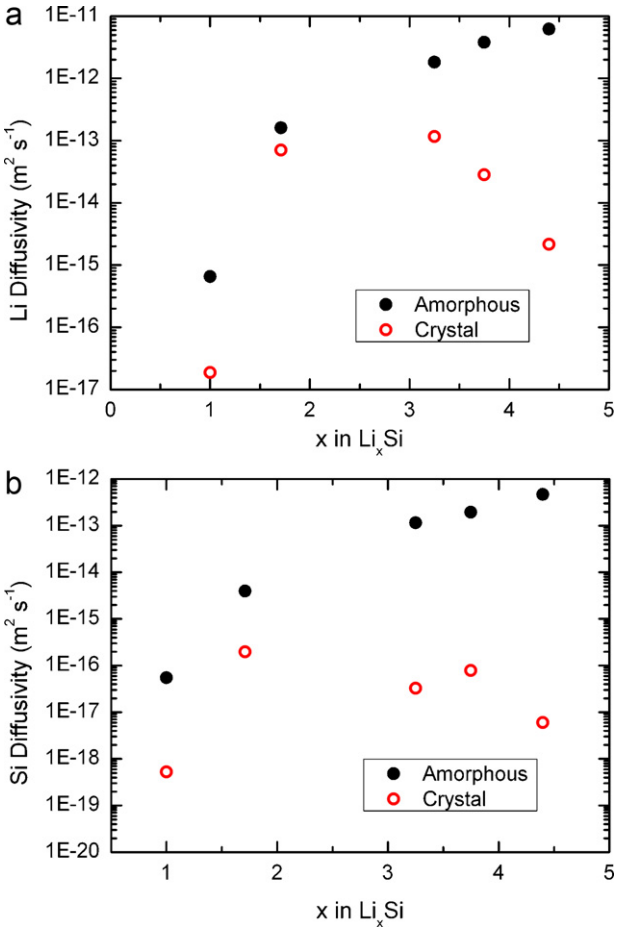

Fig. 8. Diffusivity of (a) Li and (b) Si atoms in both amorphous and crystalline Li_xSi alloys at 300 K.

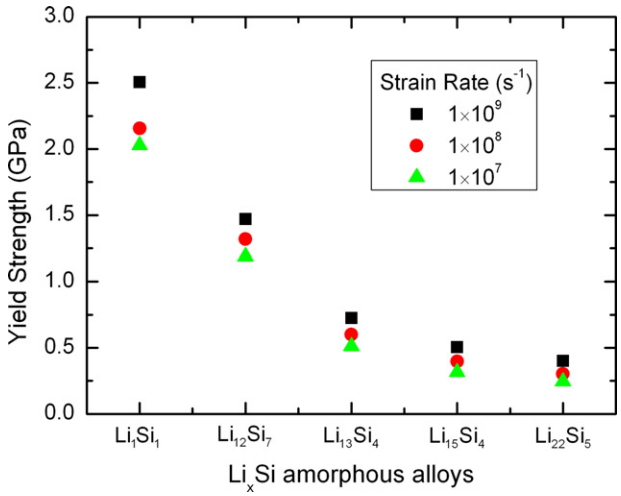

Fig. 10. Yield strength as a function of Li concentration in amorphous Li_xSi alloys under different strain rates.

Table A1
Optimized parameters in the 2NN MEAM potential for Li [52] and Si. The units of the cohesive energy E_c and equilibrium nearest neighbor distance r_e are in eV and Å, respectively.

	E_c	r_e	α	d	A	$\beta^{(0)}$	$\beta^{(1)}$	$\beta^{(2)}$	$\beta^{(3)}$	$t^{(1)}$	$t^{(2)}$	$t^{(3)}$	C_{max}	C_{min}
Li[52]	1.65	2.99	3.00	0.14	0.64	1.03	4.88	4.15	5.27	−1.46	4.13	−0.57	1.91	0.31
Si	4.63	2.35	4.90	0.03	0.53	3.00	7.50	0.00	3.00	1.45	7.61	−2.10	2.60	0.75
Si[45]	4.63	2.35	4.92	0.00	0.58	3.55	2.50	0.00	7.50	1.80	5.25	−2.61	2.80	1.41

Shown in Fig. 9 are the simulated room temperature (300 K) stress–strain curves under the strain rate of 10^8 for various compositions of amorphous Li_xSi. It is seen that the stress–strain curves exhibit the typical characteristics of metallic materials – an initial linear portion, then nonlinear portion. The Young's modulus can be obtained from the slop of the linear portion of the uniaxial stress–strain curve. The Young's modulus so obtained agrees well with that given in Fig. 5, which is obtained by using the stress and strain fluctuation formula [64] *via* MD simulation.

The yield strength can then be extracted from the uniaxial stress–strain curves in Fig. 9. This is done by first plotting the linear regression of the linear portion of the stress–strain curve; then plotting a parallel line with 0.2% strain offset. The intersection between this 0.2% offset line and the stress–strain curve gives the yield strength. The yield strength so obtain is shown in Fig. 10 as a function of Li concentration under three different strain rates.

Clearly, the yield strength is rate dependent. However, the data seem to show that, even with 2 orders of magnitude difference in strain rate, the yield strength does not change significantly, albeit this observation is made based on data at extremely high strain rates. To obtain accurate quasi-static yield strength, more studies are needed.

4. Summary and concluding remarks

A 2NN MEAM interatomic potential for the Li–Si system is developed in this paper by fitting the 13 adjustable parameters in the potential function to a number of physical properties of the Li–Si alloys. These properties are obtained by using the first principles calculations, and the fitting is done by using the particle swarm optimization method.

Validity and accuracy of the new 2NN MEAM potential is demonstrated by computing primary structural properties for both crystalline and amorphous Li_xSi alloys, as well as simulating the transition from disordered to ordered states of the atomistic structure.

The validated 2NN MEAM potential is then used to calculate several thermomechanical properties of the Li–Si systems including the elastic modulus, diffusivity of Li in Li_xSi alloys, and the plastic yield strength. The results show that these properties are all concentration dependent, *i.e.*, they are function of x in Li_xSi.

This new interatomic potential will be powerful tool for the modeling and simulation of fracture failure of Si-based anode in Li-ion batteries. It enables us to validate the various continuum models on Li insertion; it can be used to estimate some of the material properties that are difficult to obtain experimentally; and it gives us a mean to study the microstructural mechanisms of fracture and failure.

Acknowledgements

This work is supported by ISEN Booster Award at Northwestern University.

Appendix A. 2NN MEAM potential for Si

Using the same method described in Ref. [52], we have developed a 2NN MEAM potential for pure Si. The parameters in this 2NN MEAM potential are somewhat different from those given in Ref. [45], see Table A1. The elastic constants and vacancy energies calculated by our 2NN MEAM potential are consistent with the values given by Baskes [43], Lee [45] and Timonova [71]. However, our MEAM potential provides a better description of the relation between energy and Si–Si nearest neighbor distance for more reference structures, as illustrated in Fig. A1, where the total energies of the auxiliary structures are plotted *versus* nearest neighbor distance varying from 2.0 to 3.5 Å.

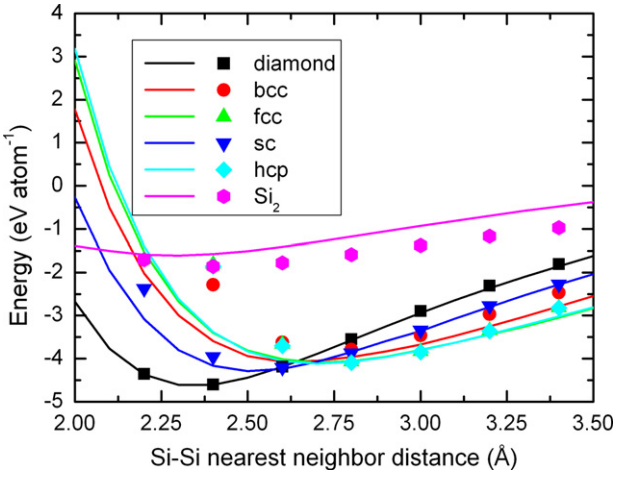

Fig. A1. Comparison between the MD results (data points) and *ab initio* calculation (solid curve). Energies of several crystals and molecular structures are plotted *versus* the Si–Si nearest-neighbor distance.

References

[1] B. Scrosati, J. Garche, Journal of Power Sources 195 (2010) 2419.
[2] M.N. Obrovac, L. Christensen, D.B. Le, J.R. Dahnb, Journal of the Electrochemical Society 154 (2007) A849.
[3] K. Kang, H.S. Lee, D.W. Han, G.S. Kim, D. Lee, G. Lee, Y.M. Kang, M.H. Jo, Applied Physics Letters 96 (2010) 053110.
[4] L.F. Cui, R. Ruffo, C.K. Chan, H.L. Peng, Y. Cui, Nano Letters 9 (2009) 491.
[5] V.L. Chevrier, J.R. Dahn, Journal of the Electrochemical Society 156 (2009) A454.
[6] C.K. Chan, H.L. Peng, G. Liu, K. McIlwrath, X.F. Zhang, R.A. Huggins, Y. Cui, Nature Nanotechnology 3 (2008) 31.
[7] Y.M. Kang, S.B. Suh, Y.S. Kim, Inorganic Chemistry 48 (2009) 11631.
[8] P. Limthongkul, Y.I. Jang, N.J. Dudney, Y.M. Chiang, Acta Materialia 51 (2003) 1103.
[9] V.L. Chevrier, J.W. Zwanziger, J.R. Dahn, Canadian Journal of Physics 87 (2009) 625.
[10] J. Li, J.R. Dahn, Journal of the Electrochemical Society 154 (2007) A156.
[11] M.N. Obrovac, L. Christensen, Electrochemical, Solid State Letters 7 (2004) A93.
[12] H. Guo, H.L. Zhao, C.L. Yin, W.H. Qiu, Materials Science and Engineering B 131 (2006) 173.
[13] C.K. Chan, R. Ruffo, S.S. Hong, R.A. Huggins, Y. Cui, Journal of Power Sources 189 (2009) 34.
[14] B. Laik, L. Eude, J.P. Pereira-Ramos, C.S. Cojocaru, D. Pribat, E. Rouviere, Electrochimica Acta 53 (2008) 5528.
[15] M.H. Park, M.G. Kim, J. Joo, K. Kim, J. Kim, S. Ahn, Y. Cui, J. Cho, Nano Letters 9 (2009) 3844.
[16] H. Ma, F.Y. Cheng, J. Chen, J.Z. Zhao, C.S. Li, Z.L. Tao, J. Liang, Advanced Materials 19 (2007) 4067.
[17] Y. Yang, M.T. McDowell, A. Jackson, J.J. Cha, S.S. Hong, Y. Cui, Nano Letters 10 (2010) 1486.
[18] R. Ruffo, S.S. Hong, C.K. Chan, R.A. Huggins, Y. Cui, Journal of Physical Chemistry C 113 (2009) 11390.
[19] J. Cho, Journal of Materials Chemistry 20 (2010) 4009.
[20] V.B. Shenoy, P. Johari, Y. Qi, Journal of Power Sources 195 (2010) 6825.

[21] V.A. Sethuraman, M.J. Chon, M. Shimshak, V. Srinivasan, P.R. Guduru, Journal of Power Sources 195 (2010) 5062.
[22] R. Teki, M.K. Datta, R. Krishnan, T.C. Parker, T.M. Lu, P.N. Kumta, N. Koratkar, Small 5 (2009) 2236.
[23] J.P. Maranchi, A.F. Hepp, P.N. Kumta, Electrochemical, Solid State Letters 6 (2003) A198.
[24] J. Christensen, J. Newman, Journal of Solid State Electrochemistry 10 (2006) 293.
[25] Y.T. Cheng, M.W. Verbrugge, Journal of the Electrochemical Society 157 (2010) A508.
[26] J. Christensen, Journal of the Electrochemical Society 157 (2010) A366.
[27] J. Christensen, J. Newman, Journal of the Electrochemical Society 153 (2006) A1019.
[28] S. Golmon, K. Maute, M.L. Dunn, Computers and Structures 87 (2009) 1567.
[29] T.K. Bhandakkar, H.J. Gao, International Journal of Solids and Structures 47 (2010) 1424.
[30] F.Q. Yang, Journal of Applied Physics 107 (2010) 103516.
[31] Y.T. Cheng, M.W. Verbrugge, Journal of Applied Physics 104 (2008) 083521.
[32] H. Haftbaradaran, H.J. Gao, W.A. Curtin, Applied Physics Letters 96 (2010) 091909.
[33] D.L. Olmsted, R. Phillips, W.A. Curtin, Modelling and Simulation in Materials Science and Engineering 12 (2004) 781.
[34] H. Haftbaradaran, J. Song, W.A. Curtin, H.J. Gao, Journal of Power Sources 196 (2011) 361.
[35] K.J. Zhao, M. Pharr, S.Q. Cai, J.J. Vlassak, Z.G. Suo, Journal of the American Ceramic Society 94 (2011) S226.
[36] K.J. Zhao, M. Pharr, J.J. Vlassak, Z.G. Suo, Journal of Applied Physics 109 (2011) 016110.
[37] G. Henkelman, H. Jonsson, Journal of Chemical Physics 113 (2000) 9978.
[38] G. Henkelman, B.P. Uberuaga, H. Jonsson, Journal of Chemical Physics 113 (2000) 9901.
[39] X.H. Liu, H. Zheng, L. Zhong, S. Huan, K. Karki, L.Q. Zhang, Y. Liu, A. Kushima, W.T. Liang, J.W. Wang, J.H. Cho, E. Epstein, S.A. Dayeh, S.T. Picraux, T. Zhu, J. Li, J.P. Sullivan, J. Cumings, C.S. Wang, S.X. Mao, Z.Z. Ye, S.L. Zhang, J.Y. Huang, Nano Letters 11 (2011) 3312.
[40] K. Rhodes, N. Dudney, E. Lara-Curzio, C. Daniel, Journal of the Electrochemical Society 157 (2010) A1354.
[41] X.H. Liu, J.Y. Huang, Energy and Environmental Science 4 (2011) 3844.
[42] S. Huang, T. Zhu, Journal of Power Sources 196 (2011) 3664.
[43] M.I. Baskes, Physical Review B 46 (1992) 2727.
[44] B.J. Lee, M.I. Baskes, H. Kim, Y.K. Cho, Physical Review B 64 (2001) 184102.
[45] B.J. Lee, Calphad-Computer Coupling of Phase Diagrams and Thermochemistry 31 (2007) 95.
[46] Y.M. Kim, N.J. Kim, B.J. Lee, Calphad-Computer Coupling of Phase Diagrams and Thermochemistry 33 (2009) 650.
[47] J. Kennedy, R. Eberhart, IEEE International Conference on Neural Networks Proceedings (1995) 1942.
[48] Z.H. Cui, J.C. Zeng, 4th International Conference on Routh Sets and Current Trends in Computing, 2004, p. 762.
[49] Z.H. Cui, J.C. Zeng, G.J. Sun, International Journal of Innovative Computing Information and Control 2 (2006) 1365.
[50] V.L. Chevrier, J.W. Zwanziger, J.R. Dahn, Journal of Alloys and Compounds 496 (2010) 25.
[51] H. Kim, C.Y. Chou, J.G. Ekerdt, G.S. Hwang, Journal of Physical Chemistry C 115 (2011) 2514.
[52] Z. Cui, F. Gao, Z. Cui, J. Qu, Modelling and Simulation in Materials Science and Engineering 20 (2012) 015014.
[53] J.H. Rose, J.R. Smith, F. Guinea, J. Ferrante, Physical Review B 29 (1984) 2963.
[54] J.G. Vlachogiannis, K.Y. Lee, Expert Systems with Applications 36 (2009) 10802.
[55] O. Begambre, J.E. Laier, Advances in Engineering Software 40 (2009) 883.
[56] S. Chen, C.J. Harris, X. Hong, B.L. Luk, International Journal of Bio-inspired Computation 1 (2009) 246.
[57] W.S. Lee, Y.T. Chen, T.H. Wu, Applied Energy 86 (2009) 1589.
[58] http://lammps.sandia.gov.
[59] S. Plimpton, Journal of Computational Physics 117 (1995) 1.
[60] S.J. Clark, M.D. Segall, C.J. Pickard, P.J. Hasnip, M.J. Probert, K. Refson, M.C. Payne, Zeitschrift Fur Kristallographie 220 (2005) 567.
[61] P. Johari, Y. Qi, V.B. Shenoy, Nano Letters 11 (2011) 5494.
[62] N. Swaminathan, J. Qu, Y. Sun, Philosophical Magazine 87 (2007) 1705.
[63] N. Swaminathan, J. Qu, Modelling and Simulation in Materials Science and Engineering 17 (2009) 045006.
[64] Z.W. Cui, Y. Sun, J. Li, J.M. Qu, Physical Review B 75 (2007) 214101.
[65] S. Tim, Properties of Amorphous Silicon and Its Alloys, Institution of Electrical Engineers, 1998.
[66] R.J. Bondi, S. Lee, G.S. Hwang, Physical Review B 81 (2010) 195207.
[67] R.L.C. Vink, G.T. Barkema, W.F. van der Weg, N. Mousseau, Journal of Non-Crystalline Solids 282 (2001) 248.
[68] N. Ding, J. Xu, Y.X. Yao, G. Wegner, X. Fang, C.H. Chen, I. Lieberwirth, Solid State Ionics 180 (2009) 222.
[69] Z.W. Cui, Y. Sun, Y.J. Chen, J.M. Qu, Solid State Ionics 187 (2011) 8.
[70] Z. Cui, F. Gao, Z. Cui, J. Qu, Journal of the Mechanics and Physics of Solids (2011), submitted.
[71] M. Timonova, B.J. Thijsse, Modelling and Simulation in Materials Science and Engineering 19 (2011) 015003.